

# Numerical Study of Fluid Flow, Heat Transfer and Parameter Coupling in a Spider Web Microchannel Heat Sink

L. Chen<sup>1</sup>, Y. Kang<sup>†1</sup>, and S. Kao-Walter<sup>2,3</sup>

<sup>1</sup> School of Mechanical and Electrical Engineering, Kunming University of Science and Technology, Yunnan Province, 650093, China

<sup>2</sup> Department of Mathematics and Natural Sciences, Blekinge Institute of Technology, Karlskrona 37179, Sweden

<sup>3</sup> Institute of Intelligent Manufacturing and Control Engineering, Shanghai Polytechnic University, Shanghai, 201209, China

†Corresponding author email: [yuchi.kang@kust.edu.cn](mailto:yuchi.kang@kust.edu.cn)

## ABSTRACT

The microchannel heat sink is a commonly used structure in mechanical cooling systems for microelectronics. Based on bionics, a simplified heat sink with a spider-web design is proposed in this paper. Under the condition of bottom heat flux  $q = 100 \text{ W/cm}^2$  and Reynolds number ( $Re$ ) = 442–884, the influence of three parameters (main channel width, branch width and rib width) on the performance of a spider web microchannel heat sink (SW-MCHS) under different  $Re$  conditions was numerically analyzed by computational fluid dynamics. The results showed that the main channel had the greatest influence on the Nusselt number ( $Nu$ ) and the Euler number ( $Eu$ ); With the increase of main channel width,  $Nu$  increased by 46.97%, and  $Eu$  decreased by 31.74%. Rib width had the smallest influence on  $Nu$  and  $Eu$ ; With the increase of rib width,  $Nu$  decreased by 7.18%, and  $Eu$  decreased by 12.00%. Based on the research results, the correlations for predicting  $Nu$  and  $Eu$  of the SW-MCHS were fitted; the  $R_{adj}^2$  values for the two correlations were 0.9523 and 0.9246, respectively. These fitting correlations could be used to predict  $Nu$  and  $Eu$  for the SW-MCHS. The present study has contributed to advancing the applications of microchannel heat sinks and enhancing the cooling efficiency of mechanical microelectronics cooling systems.

## Article History

Received November 22, 2024

Revised February 17, 2025

Accepted February 18, 2025

Available online May 5, 2025

## Keywords:

Spider web microchannel heat sink

Heat transfer

Flow characteristics

Correlation fitting

Computational fluid dynamics

## 1. INTRODUCTION

With the rapid advancement of integration and miniaturization in electronic devices, the number of transistors in integrated circuits has risen substantially. Consequently, as device performance has improved, the heat flux experienced by these electronics has also escalated, making heat dissipation a pivotal issue in current research (Li et al., 2019; Pan et al., 2019; Huang et al., 2020; Niu et al., 2021; Wu et al., 2022). The heat flux density of electronic equipment such as CPUs, for example, has reached  $100 \text{ W/cm}^2$ . Therefore, the boundary conditions of the numerical simulation in this study were performed with  $100 \text{ W/cm}^2$  as an example (Sharma et al., 2012; Soheli Murshed & Nieto De Castro, 2017; Patil & Hotta, 2018; Qi et al., 2022). Known heat dissipation methods are air cooling, water cooling, semiconductor refrigeration, heat pipe cooling and the microchannel heat sink (MCHS). Because of its small size, compact structure and high heat dissipation efficiency, the MCHS has become a popular choice in solving the heat dissipation of microdevices (Lu

& Zhai, 2019; Gao et al., 2024; Zhu et al., 2024).

A conventional MCHS generates a thick boundary layer, and insufficient mixing of cold and hot fluids leads to poor heat exchange capacity. Thus, a conventional MCHS is unable to meet current heat transfer requirements. Some investigators have applied bionic structures to aerospace, lithium battery development and other fields and have achieved promising results. The application of bionic structures in these fields has also provided new ideas for the design of heat sink structures (Kumar, 2019; Li et al., 2020; Zhang et al., 2024a).

Some investigators have studied bionic MCHS configurations. In comparison to traditional MCHS structures, various bionic MCHSs have demonstrated improved performance (Tan et al., 2019a; Wang et al., 2021a; Yang et al., 2021; Huang et al., 2024; Yao et al., 2024; Zhang et al., 2024). The effects of different heat sinks on the heat transfer performance of a chip during cooling have been studied, and the results have shown that the spider web microchannel heat sink (SW-MCHS)

NOMENCLATURE			
$W_m$	main channel width	$\lambda$	molecular free path
$W_b$	branch width	$D_h$	hydraulic diameter
$W_r$	rib width	$\rho$	density
$P$	static pressure of water	$\rho_f$	average density of water
$V$	vector velocity of flow fluid	$C_{p f}$	specific heat capacity of water with constant pressure
$L$	length of the middle channel	$Po$	Poiseuille number
$L_0$	inner tangent radius of the smallest regular hexagon	$F$	friction coefficient
$L_R$	inner tangent radius of the first-level channel regular hexagon	$Kn$	Knudsen number
$L_{R+1}$	inner tangent radius of the remaining levels	$\mu_f$	dynamic viscosity of water
$Re$	Reynolds number	$\lambda_f$	thermal conductivity of water
$\lambda_s$	solid thermal conductivity	$T_s$	solid temperature
$T_f$	temperature of water	$Eu$	Euler number
$Nu$	Nusselt number		

has demonstrated the best heat transfer performance among the different structures proposed (Tan et al., 2019b). Therefore, the SW-MCHS has been studied further. Some scholars have applied topological optimization to the SW-MCHS and concluded that the structures generated by topological optimization are superior to ordinary structures (Han et al., 2021). Other investigators have studied the influence of different parameters on the performance of SW-MCHSs (Wang et al., 2021b; Rong et al., 2023).

In summary, many groups have studied the heat transfer characteristics of the SW-MCHS, but most studies have only shown that the SW-MCHS has better performance compared with other MCHS configurations; parameter studies have been relatively rare (Wu et al., 2018; Li et al., 2021a). Based on the appealing effects of the spider-web structure, the SW-MCHS was chosen to study the thermal performance of CPU heat dissipation. First, structural design and theoretical analysis of SW-MCHS were performed. Second, the influences of different parameters on heat sink performance were assessed. Finally, the coupling relationships between each parameter and the Nusselt number ( $Nu$ ) and Euler number ( $Eu$ ) were analyzed, and the correlations of  $Nu$  and  $Eu$  were fitted.

## 2. DESIGN OF THE SPIDER WEB MICROCHANNEL HEAT SINK

A spider web with multiple branches has useful distribution characteristics. To simplify the geometry, the SW-MCHS was designed as a regular hexagon with the branches at each level being parallel to one another, as shown in Fig. 1. The SW-MCHS contains only one diagonal flow channel, implying one inlet and one outlet, in order to avoid energy loss caused by multiple entrances and exits. The structure extends outward on both sides of the main channel, diverting the fluid from the inlet into multiple stages of branching channels, which subsequently flow out at the outlet through all levels of the channel system. The longest channel, in the middle of the model, is designated as the main channel. The hexagonal channel is designated as the branch, and the portion

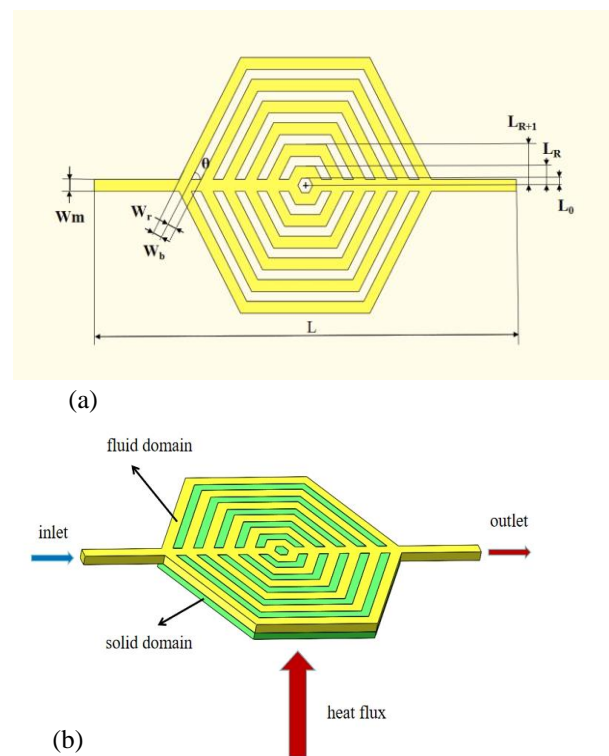


**Fig. 1 Schematic diagrams of the spider web microchannel heat sink (SW-MCHS). (a) Top view of the SW-MCHS geometry and parameters. (b) 3D schematic diagram of the SW-MCHS**

between branches is designated as the rib. The angle  $\theta$  between the branch and the main channel is  $60^\circ$ . The width of the main channel, the branch and the rib are termed  $W_m$ ,  $W_b$  and  $W_r$ , respectively. The height of the branch is 0.2 mm. The length of the main channel is  $L$ , the inner tangent radius of the smallest regular hexagon is  $L_0$ , the inner tangent radius of the first-level channel regular hexagon is  $L_R = L_0 + W_b$ , and the inner tangent radius of the remaining levels at each level follows the equation  $L_{R+1} = L_R + W_b + W_r$ , where  $L_0 = 0.15$  mm. Detailed parameters are shown in Table 1.

**Table 1 Geometrical parameters of the structure**

Geometrical parameters	Value (mm)
Main channel width ( $W_m$ )	0.15, 0.2, 0.25, 0.3, 0.35
Branch width ( $W_b$ )	0.1, 0.175, 0.25, 0.325, 0.4
Rib width ( $W_r$ )	0.15, 0.175, 0.2, 0.225, 0.25
Height of the fluid domain ( $H$ )	0.2

### 3. NUMERICAL METHODS

#### 3.1 Continuum Hypothesis

The Knudsen number ( $Kn$ ) is a dimensionless number used to determine whether a continuity hypothesis is valid. A value of  $Kn$  less than 0.001 indicates that the continuity hypothesis is valid, which means the Navier–Stokes equation, the energy equation and the boundary conditions without velocity slip and temperature jump are valid under macroscopic conditions (Service, 1998). The size range of heat sink is usually defined as the hydraulic diameter  $D_h = 0.001–1$  mm;  $D_h$  was less than 0.3 mm for all heat sink structures assessed in this study.

$Kn$  is expressed as follows:

$$Kn = \frac{\lambda}{D_h} \quad (1)$$

where  $\lambda$  is the molecular free path in mm.  $D_h$  is the hydraulic diameter in mm, which can be calculated as follows:

$$D_h = \frac{2W_bH}{(W_b + H)} \quad (2)$$

where  $H$  is the height of the structure.

The average free path of water molecules is approximately  $10^{-10}$  m, and the hydraulic diameter of the heat sink is brought into the equation, and  $Kn$  is far less than 0.001. Therefore, the continuum hypothesis remains valid for the microchannel structure proposed in this paper.

#### 3.2 Governing Equations

Since fluid flow and heat transfer are included in the present study, both continuity equation, momentum equation and energy equation should be solved in the iteration way.

Continuity equation:

$$\nabla \cdot \mathbf{V} = 0 \quad (3)$$

where  $\mathbf{V}$  is the vector velocity of flow fluid in m/s.

Momentum equation:

$$\rho_f (\mathbf{V} \cdot \nabla \mathbf{V}) = -\nabla P + (\mu_f \cdot \nabla \nabla) \quad (4)$$

where  $\rho_f$  is the average density of water in  $\text{kg/m}^3$ ,  $P$  is the static pressure of water in Pa and  $\mu_f$  is the dynamic viscosity of water in  $\text{kg/(m}\cdot\text{s)}$ .

Energy equation for fluid domain:

$$\rho_f C_{p_f} \mathbf{V} \cdot \nabla T_f = \nabla \cdot (\lambda_f \nabla T_f) \quad (5)$$

where  $C_{p_f}$  is the specific heat capacity of water with constant pressure in  $\text{kJ/(kg}\cdot\text{K)}$ ,  $\lambda_f$  is the thermal conductivity of water in  $\text{W/(m}\cdot\text{K)}$  and  $T_f$  is the temperature of water in K.

Energy equation for solid domain:

$$\nabla \cdot (\lambda_s \cdot \nabla T_s) = 0 \quad (6)$$

where  $T_s$  is the solid temperature in K and  $\lambda_s$  is the solid thermal conductivity in  $\text{W/(m}\cdot\text{K)}$ .

Other necessary parameters were calculated as follows:

The Reynolds number ( $Re$ ) is a variable representing the ratio of inertial force to viscous force in fluids. Therefore,  $Re$  is usually used to determine whether a fluid flow is laminar or turbulent.  $Re$  can be expressed as follows:

$$Re = \frac{\rho_f V_{in} D_h}{\mu_f} \quad (7)$$

where  $V_{in}$  is the inlet velocity in m/s.

$Nu$  represents the ratio of convective heat transfer across the boundary to conduction heat.  $Nu$  is calculated using the following equation:

$$Nu = \frac{h D_h}{\lambda_f} \quad (8)$$

where  $h$  represents the local convective heat transfer coefficient, which can be calculated as follows:

$$h = \frac{q A_h}{A_c (T_s - T_f)} \quad (9)$$

where  $q$  is the heat flux,  $A_h$  represents the heating area and  $A_c$  represents the convective heat transfer area.

$Eu$  represents the ratio of local pressure decrease to kinetic energy. It reflects the relative magnitude of momentum loss during flow.  $Eu$  is calculated by the following equation:

$$Eu = \frac{2\Delta P}{\rho_f V_{max}^2} \quad (10)$$

where  $V_{max}$  is the maximum velocity of fluid in m/s and  $\Delta P$  is the pressure drop, which is defined by the following equation:

$$\Delta P = P_{in} - P_{out} \quad (11)$$

where  $P_{in}$  is the pressure of the inlet and  $P_{out}$  is the pressure of the outlet.

#### 3.3 Boundary Conditions

To solve the governing equations above, the boundary conditions were employed in numerical simulations. Considering the actual engineering conditions of the MCHS, a single-side heating method was employed for the numerical calculations. The bottom area was applied with the heat flux  $q = 100 \text{ W/cm}^2$ . The fluid–solid contact areas were set to reflect non-slip and adiabatic boundary conditions, which were applied to other walls of the

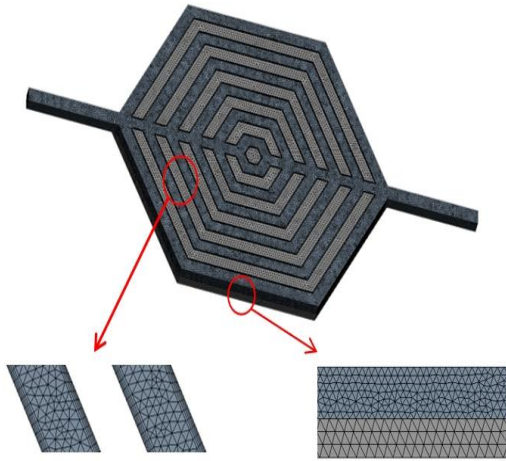


**Fig. 2** Meshing of the spider web microchannel heat sink.

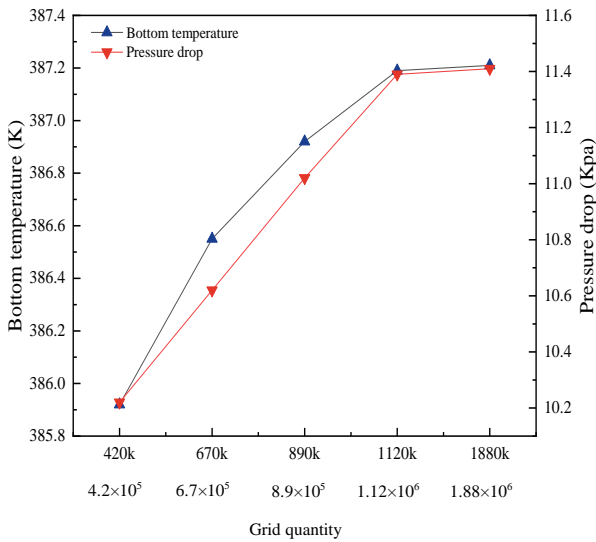


**Fig. 3** Results of the grid independence test

computational domain. The velocity to the inlet was supplied with values of 2, 2.5, 3, 3.5 and 4 m/s, respectively. The pressure to the outlet was set to  $1.03 \times 10^3$  KPa.

### 3.4 Grid Independence

The geometry was divided into two parts, namely the solid domain and the fluid domain. To conserve numerical resources, the mesh size of the solid domain was set as slightly larger than that of the fluid domain because the solid domain only contained the heat conduction. The fluid–solid contact area was encrypted to improve the quality of the solution. The detailed meshing is shown in Fig. 2.

A structure with a main channel width of 0.25 mm, a branch width of 0.25 mm and a rib width of 0.3 mm was selected as an example to verify grid independence. In this

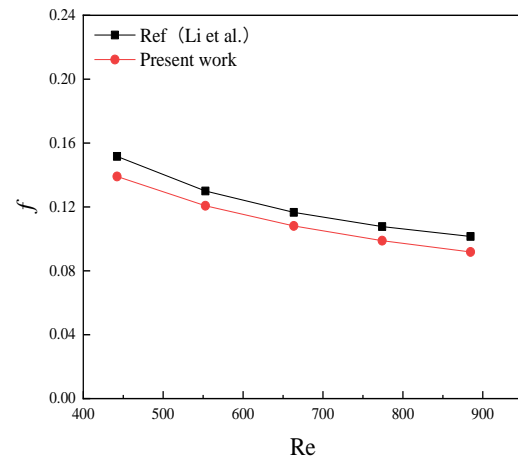


**Fig. 4.** Comparison of the friction coefficients calculated from the empirical formula of Li et al. (2024b) and those of the simulations in the present work

study, five sets of grids with different sizes were used to verify the grid independence. By comparing the differences of the results, the appropriate number of grids was selected to ensure the reliability of the results. The SW-MCHS was divided into five different groups of grids with different mesh sizes, and the numbers of grids were  $4.2 \times 10^5$ ,  $6.7 \times 10^5$ ,  $8.9 \times 10^5$ ,  $1.12 \times 10^6$ ,  $1.88 \times 10^6$ , respectively. Under the working conditions of  $Re = 442.31$ , the five groups of grids were numerically simulated; the calculation results of the pressure drop are shown in Fig. 3. A total number of  $1.12 \times 10^6$  grids was selected.

### 3.5 Model Verification

To verify the numerical model, the numerical results were compared with those of an empirical formula (Li et al., 2024b). The friction coefficient formula for laminar flow in a microchannel is as follows:

$$f = \frac{\sqrt{\left(\frac{3.2ReD_h}{L}\right)^2 + P_o^2}}{Re} \quad (12)$$

$$P_o = 96(1 - 1.3553X + 1.9467X^2 + 1.7012X^3 + 0.9564X^4 - 0.2573X^5) \quad (13)$$

where  $X$  is the aspect ratio of the microchannel.

In this analysis, water was used as the medium for numerical simulation, the inlet temperature was 293 K, and  $Re$  ranged from 442 to 884. The results of a comparison between the calculated values and the simulated values are shown in Fig. 4. The maximum error between the friction coefficient calculated by numerical calculation and the friction coefficient calculated by empirical formula was 9.56%, which is due to the fact that Li’s empirical formula pertains specifically to a straight channel, which differed from the current scenario.

## 4. RESULTS AND DISCUSSION

### 4.1 Velocity and TEMPERATURE DISTRIBUTION

The main channel width, the branch width and the rib width of the geometrical model studied here were 0.25 mm,

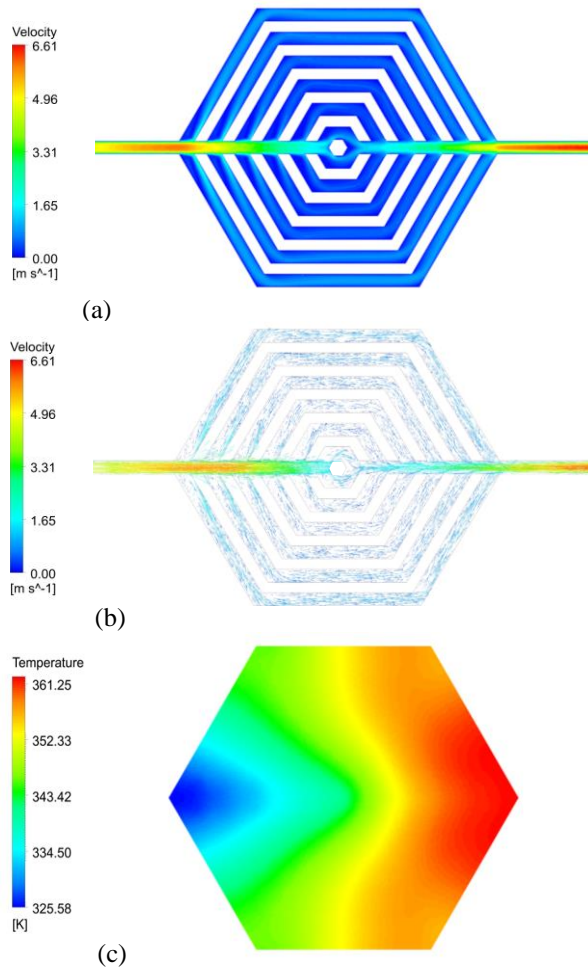


**Fig. 5 (a) Velocity distribution inside the fluid region of the cross section at a height of 0.1 mm. (b) Velocity vector distribution inside the fluid region of the cross section at a height of 0.1 mm. (c) Bottom temperature distribution**

0.25 mm and 0.2 mm, respectively. The inlet velocity was 4 m/s.

The velocity distribution inside the fluid region of the cross section at a height of 0.1 mm is displayed in Fig. 5(a). The velocity was nearly symmetric and ranged from 0 to 6.48 m/s. The velocity decreased gradually along the main channel axis from the inlet to the core, then increased again. The maximum velocity occurred at the intersections between the main channel and branches. The velocity distribution in the branches was relatively lower than in the main channel. A notable observation is that velocity at the inner branches was lower than at the outer branches. These findings are consistent with those of Rong et al. (2023).

The velocity vector distribution inside the fluid region of the cross section at a height of 0.1 mm is displayed in Fig. 5(b). It can be seen from this graphic that in the second half of the flow, as the fluid of the branch gradually mixed with the fluid of the main channel, the velocity of the fluid in the main channel gradually increased, enhancing the heat transfer effect.

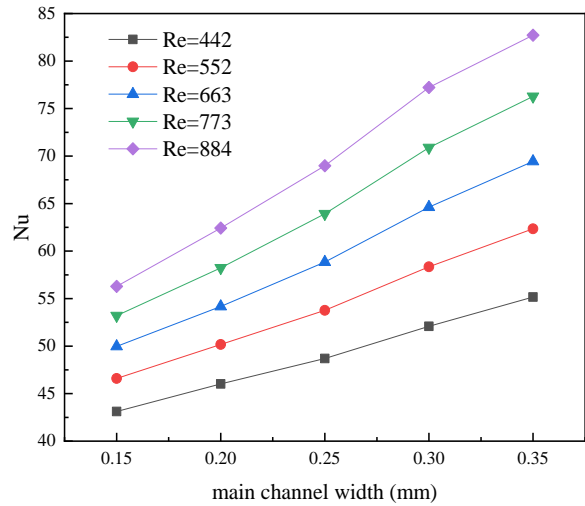


**Fig. 6 Effects of main channel width and Reynolds number (*Re*) on the Nusselt number (*Nu*).** (*Nu*)

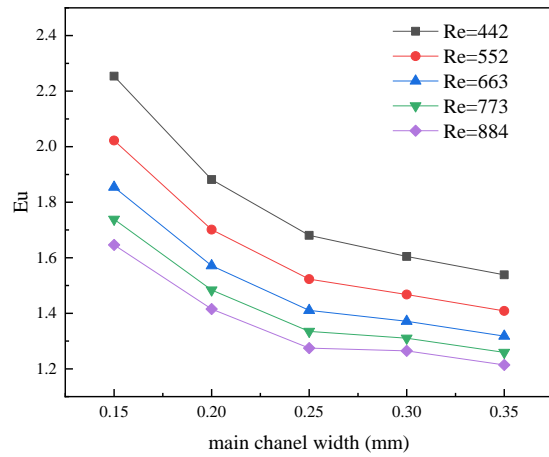


**Fig. 7 Effects of main channel width and Reynolds number (*Re*) on the Euler number (*Eu*)**

The temperature distribution of the bottom surface is presented in Fig. 5(c). In general, the temperature was low at the inlet region and high at the outlet region as the fluid moved from upstream to downstream. The maximum temperature was 361.25 K at the exit region, and the minimum temperature was 325.58 K at the inlet region.

#### 4.2 Effect of Main Channel Width on Performance

Figure 6 presents the *Nu* variations as a function of the main channel width with varying *Re*. As is evident from the figure, *Nu* exhibited an upward trend with the increase in main channel width. Taking the parameters *Re* = 442, *W<sub>b</sub>* = 0.25 mm and *W<sub>r</sub>* = 0.2 mm as an example, as the main channel width expanded from 0.15 mm to 0.35 mm, *Nu* progressively increased from 43.12 to 46.02, 48.70, 52.08 and finally 55.17. At a constant *Re*, the augmentation in *Nu* due to the widened main channel width indicates an improvement in the heat transfer performance of the SW-MCHS. This enhancement can be attributed to the increased fluid flow into both the main channel and the branches as well as the enlarged contact area between the fluid and the solid, which collectively enhanced the heat transfer capacity. Consequently, *Nu*

varied within a range of 27.94% to 46.97% across different main channel widths. Additionally, at a fixed main channel width,  $Nu$  also rose with an increase in  $Re$ . This effect occurred because the higher velocity led to stronger disturbances, resulting in a more effective mixing process. Specifically, the maximum increase in  $Nu$  due to a higher  $Re$  reached 49.94%.

Figure 7 presents a comparative analysis of  $Eu$  as a function of increasing main channel width across various values of  $Re$ . Using the parameters  $Re = 442$ ,  $W_b = 0.25$  mm and  $W_r = 0.2$  mm as an illustrative example, the figure demonstrates that as the main channel width expanded from 0.15 mm to 0.35 mm,  $Eu$  exhibited a decreasing trend, specifically dropping from 2.25 to 1.88, 1.68, 1.60 and finally 1.54. This reduction in  $Eu$  suggests an improvement in the overall efficiency of the fluid flow within the SW-MCHS. At a constant  $Re$ , an increase in main channel width led to a greater proportion of fluid flowing through the main channel, while the flow on both sides decreased. This shift in flow distribution resulted in reduced fluid disturbance, subsequently decreasing energy loss. As depicted in the figure,  $Eu$  decreased by a range of 26.25% to 31.74% with the widening of the main channel. Conversely, at a fixed main channel width, an increase in  $Re$  led to a higher fluid flow velocity. This increased velocity enhanced the disturbance in the corner regions of the microchannels, resulting in greater flow resistance and consequently a higher  $Eu$ . The variation in  $Eu$  across different main channel widths at elevated  $Re$  values ranged between 60.51% and 63.45%.

Figure 8 illustrates the velocity and velocity vector distributions within the local main channel at various values for  $Re$ . As  $Re$  increased, the peak velocity within the channel rose accordingly. Notably, the highest velocities were observed in the latter half of the channel, attributed to the thicker boundary layer of the fluid flow. Consequently, the mainstream area diminished, leading to an enhanced extrusion velocity of the fluid. The boundary layer effect introduced a velocity gradient transitioning from the center towards the wall and progressively intensifying along the flow direction.

#### 4.3 Effect of Branch width on Performance

Figure 9 presents variations in  $Nu$  with an increase in branch width for different values of  $Re$ . Taking  $Re = 442$ ,  $W_m = 0.25$  mm and  $W_r = 0.2$  mm as an illustrative example, as the branch width increased from 0.1 mm to 0.4 mm,  $Nu$  decreased from 66.73 to 57.35, 48.70, 44.59 and 38.10, respectively, indicating a decreasing trend. Specifically, for  $Re = 442$ ,  $W_m = 0.25$  mm and  $W_b$  less than 0.25 mm, a reduction in branch width resulted in higher flow velocities. This effect enhanced the mixing between the fluid within the branch and the cooler fluid at the top, thereby improving the heat transfer effect. Conversely, when  $W_b$  exceeded 0.25 mm, an increase in channel width led to lower fluid velocities and reduced mixing, resulting in a diminished heat transfer effect. Consequently,  $Nu$  exhibited a downward trend. For the same  $Re$  and equal bottom area, as the branch width increased, the heat transfer area decreased, leading to a worsened heat dissipation effect. This effect produced a decline in  $Nu$  ranging from 40.10% to 42.90% at different values for  $Re$ .

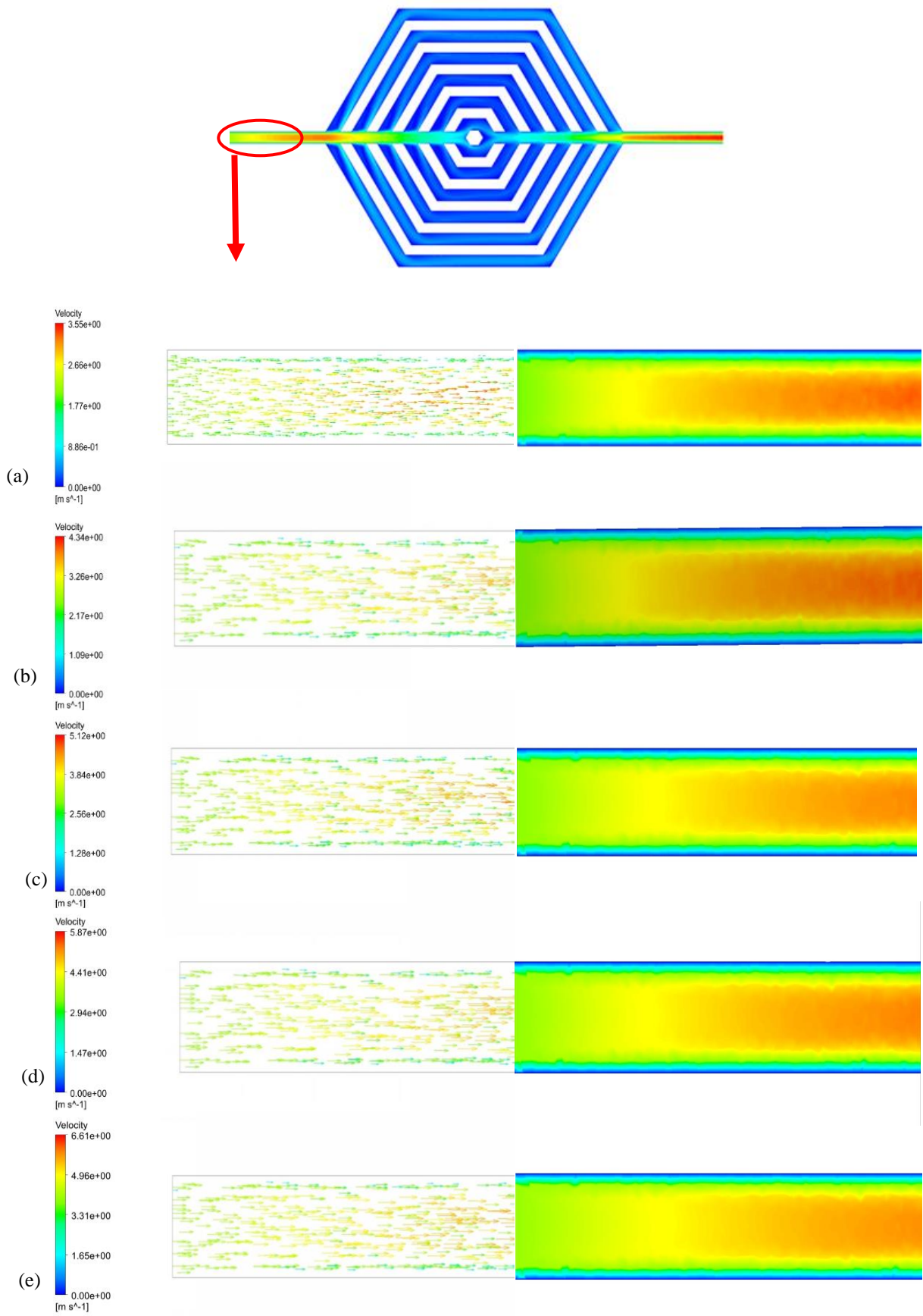
Furthermore, with an increase in  $Re$ , the low-temperature fluid in the branch mixed more thoroughly with the high-temperature fluid near the bottom and side walls, leading to a maximum increase of 42.19% in  $Nu$ .

Figure 10 depicts the variations in  $Eu$  with changes in branch width at different values for  $Re$ . Using  $Re = 442$ ,  $W_m = 0.25$  mm and  $W_r = 0.2$  mm as an example, as the branch width increased from 0.1 mm to 0.4 mm,  $Eu$  decreased from 1.99 to 1.79, 1.68, 1.45 and 1.41, respectively. When considering the same  $Re$  and equal bottom area, a smaller branch width resulted in more-level branches and a longer fluid flow distance, increasing friction loss. Additionally, as fluid flowed into a smaller branch, the constriction caused an increase in velocity, leading to enhanced disturbance within the branch and a higher pressure drop. On the other hand, as the branch width increased, the number of level branches decreased, resulting in a shorter flow distance and reduced friction loss. When  $W_b$  exceeded 0.25 mm, fluid flowing into a larger branch experienced a lower flow velocity, leading to a lower pressure drop and  $Eu$  due to the weakened fluid disturbance. Consequently, the change in  $Eu$  exhibited a downward trend. For the same  $Re$ , as the branch width increased,  $Eu$  decreased by 29.00%, 27.68%, 27.68%, 27.28% and 27.08%, respectively. With an increase in  $Re$ , the flow velocity increased and the fluid disturbance intensified, resulting in a higher pressure drop. However, the lower  $Eu$  indicates that the momentum loss was relatively lower despite the increased pressure drop.

Figure 11 shows the velocity and velocity vector distributions at the local main channel and the first, second and third branches. When the fluid flowed through the main channel into the branch, a vortex occurred at the entrance of the branch. With increased  $Re$ , the velocity of the fluid entering the branch increased, enhancing the disturbance effect caused by the vortex. It can be seen from the vector distributions that the velocity vector in the main channel was dense but that in the branch was sparse. Moreover, due to the diversion of the branches, the velocity vector in the main channel gradually decreased, resulting in increased fluid flow into the branches.

#### 4.4 Effect of Rib Width on Performance

Figure 12 illustrates a comparative analysis of  $Nu$  as the rib width increased across various  $Re$  values. Specifically, under the conditions of  $Re = 442$ ,  $W_m = 0.25$  mm and  $W_b = 0.25$  mm, an increment in rib width from 0.15 mm to 0.25 mm resulted in a progressive decrease in  $Nu$ , from 49.86 to 48.70, 48.40, 48.26 and 47.21, respectively. Within this same  $Re$  range, as the rib width expanded,  $Nu$  diminished. This reduction was accompanied by an increase in the contact area between the rib and the bottom surface, facilitating heat conduction through the rib but concurrently weakening convective heat transfer performance. Additionally, the rib width influenced the upstream area, in which a broader rib led to more fluid accumulation. This accumulation resulted in a higher velocity as the fluid split and flowed around the rib to both sides, promoting better fluid mixture along the branch and consequently enhancing convective heat transfer performance. These two factors—contact area and fluid velocity—exerted opposing influences on convective



**Fig. 8** Velocity and velocity vector distributions at the local main channel at different Reynolds number ( $Re$ ) values. (a)  $Re = 442$ ; (b)  $Re = 552$ ; (c)  $Re = 663$ ; (d)  $Re = 773$ ; (e)  $Re = 884$

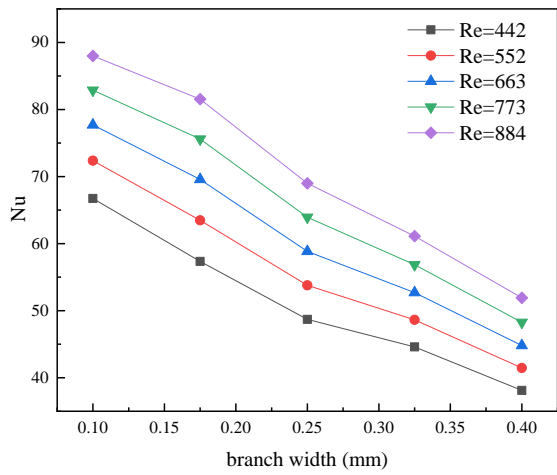


**Fig. 9** Effects of branch width and Reynolds number ( $Re$ ) on the Nusselt number ( $Nu$ )

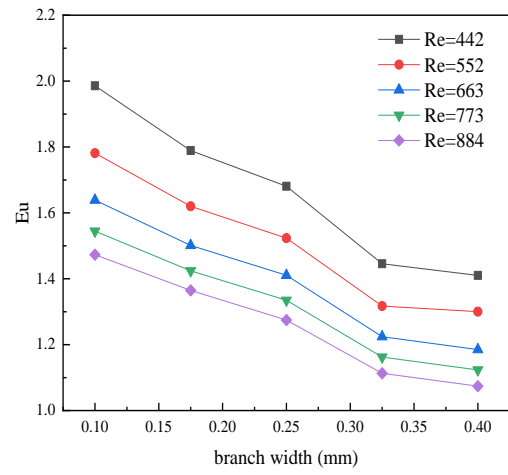


**Fig. 10** Effects of branch width and Reynolds number ( $Re$ ) on the Euler number ( $Eu$ )

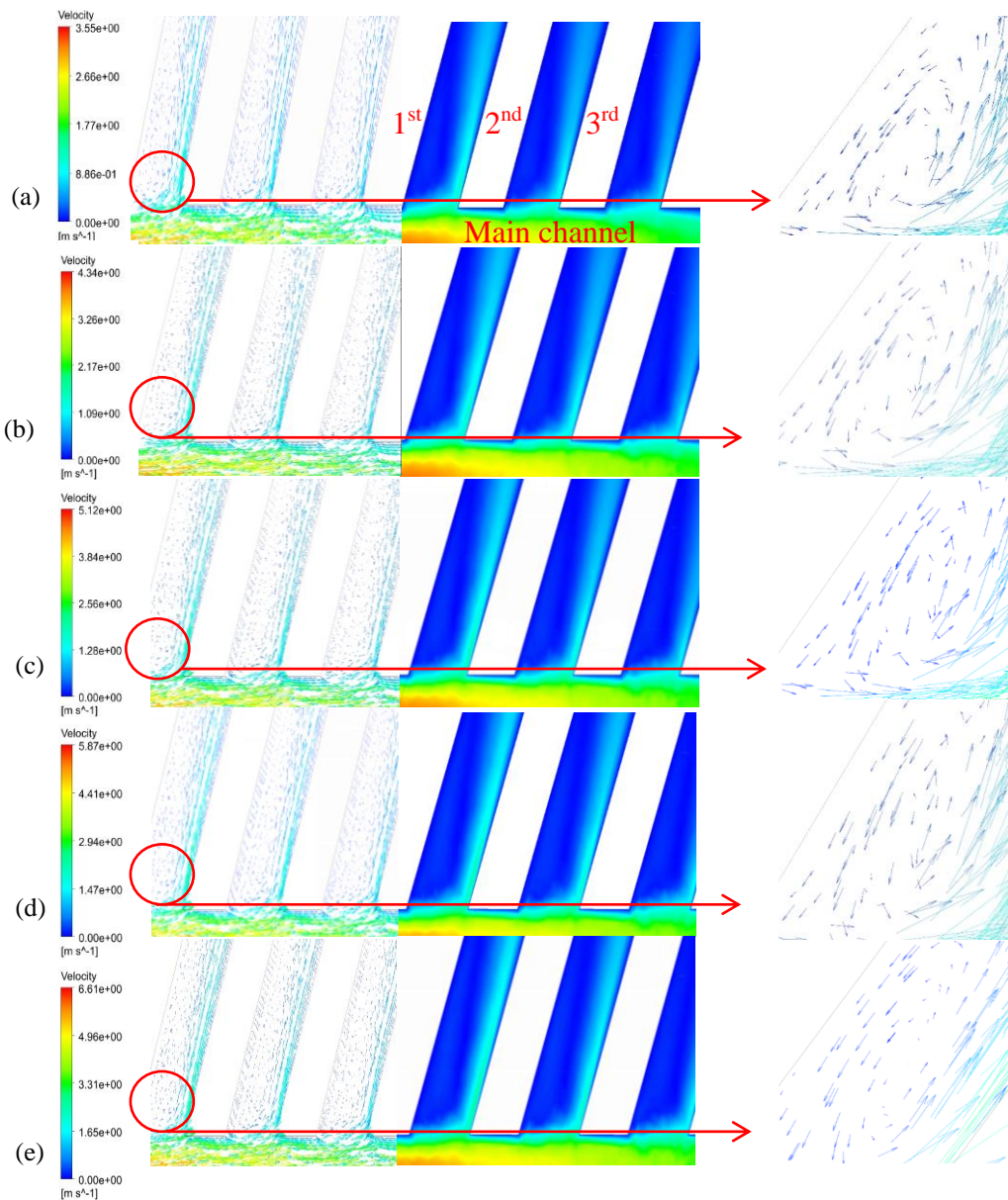


**Fig. 11** Velocity and velocity vector distributions at the local main channel and the first, second and third branches for different Reynolds number ( $Re$ ) values. (a)  $Re = 442$ ; (b)  $Re = 552$ ; (c)  $Re = 663$ ; (d)  $Re = 773$ ; (e)  $Re = 884$

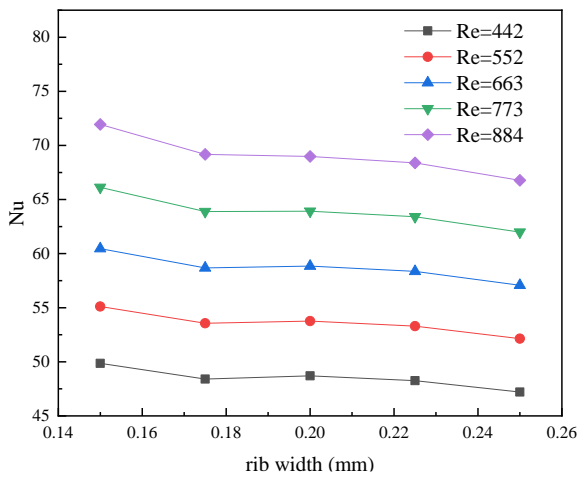


**Fig. 12** Effects of rib width and Reynolds number (*Re*) on the Nusselt number (*Nu*)

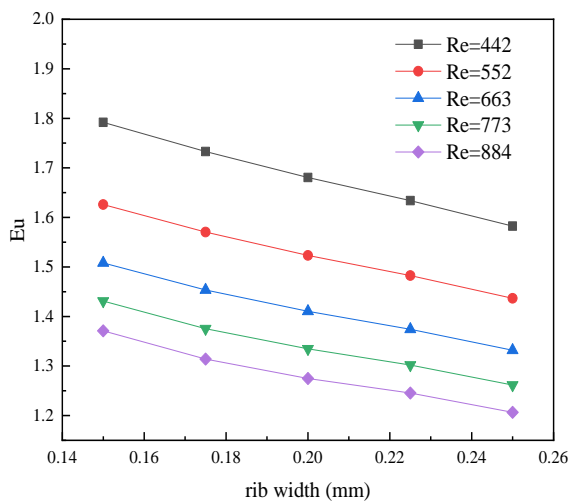


**Fig. 13** Effects of rib width and Reynolds number (*Re*) on the Euler number (*Eu*)

heat transfer performance. However, the impact of the increased contact area between the rib and the bottom surface outweighed the effect of fluid velocity, leading to an overall decrease in *Nu* by 5.32%, 5.39%, 5.59%, 6.25% and 7.18%, respectively, with each incremental increase in rib width at a constant *Re*. Furthermore, when the rib width remained constant and *Re* was increased, convective heat transfer performance was augmented, with *Nu* experiencing a maximum growth of 44.29%.

Figure 13 presents a comparative analysis of *Eu* as the rib width increased across different *Re* values. With main channel width and branch width both set at 0.25 mm, an increase in rib width from 0.15 mm to 0.25 mm resulted in a decrease in *Eu*, from 1.79 to 1.73, 1.68, 1.63 and 1.58, respectively. When considering the same *Re* and bottom area, as the rib width expanded, the number of branches diminished, leading to a shortened fluid flow path. This reduction in branches decreased the contact area between the fluid and the branches, resulting in a shorter fluid flow distance and consequently lower friction loss. Conversely, as fluid flowed into the branches, a wider rib caused more fluid to accumulate at its front, leading to a larger pressure drop. However, the influence of the number of branches

on the pressure drop outweighed the impact of the rib width. As a result, at a constant *Re*, the increase in rib width still led to an overall decreasing trend in pressure drop and friction loss, ultimately causing a reduction in *Eu*.

Figure 14 presents the velocity and velocity vector distributions at the rib's front across various *Re* values. The vector distributions illustrate that the velocity vector flowing into the branch was more concentrated compared to that of the main channel. This effect indicates that increased fluid flow into the branch enhanced the convective heat transfer performance. The acceleration effect of the ribs on the fluid was relatively minor; thus, convective heat transfer performance was primarily governed by the contact area between the fluid and the branch. This observation aligns with the analyses presented in Figs. 12 and 13.

#### 4.5 Parametric Analysis

Table 2 shows the results of computational fluid dynamics (CFD) simulation calculations in which the influences of various parameters on *Nu* and *Eu* were analyzed. The unit of main channel width, branch width and rib width is *mm*. From the analysis above, *Nu* and *Eu* can be expressed as a function of the main channel width, branch width and rib width (Rong et al., 2023). Based on the numerical results described above, two different fitted correlations could be obtained, as follows:

$$Nu = 3267.23(W_m^{1.466} + 0.255)(W_b^{-0.016} - 0.98)W_r^{-0.133} \quad (14)$$

$$Eu = 5.6 \times 10^{-4}(W_m^{-3.2} + 1044.3641)W_b^{-0.203}W_r^{-0.255} \quad (15)$$

The coefficient of determination ( $R^2$ ) can quantify how well a correlation fits a set of data. However, an intrinsic drawback of this method is that  $R^2$  always increases if a new predictor is added. The adjusted coefficient of determination ( $R_{adj}^2$ ) can be used to determine how well terms fit the data.  $R_{adj}^2$  is expressed as follows:

**Table 2** Results of CFD simulation cases

No.	Main channel width	Branch width	Rib width	<i>Nu</i>	<i>Eu</i>
1	0.15	0.25	0.2	56.29	1.65
2	0.2	0.25	0.2	62.42	1.42
3	0.25	0.25	0.2	68.99	1.27
4	0.3	0.25	0.2	77.22	1.26
5	0.35	0.25	0.2	82.72	1.21
6	0.25	0.1	0.2	87.99	1.47
7	0.25	0.175	0.2	81.54	1.36
8	0.25	0.25	0.2	68.99	1.27
9	0.25	0.325	0.2	61.11	1.11
10	0.25	0.4	0.2	51.92	1.07
11	0.25	0.25	0.15	71.94	1.37
12	0.25	0.25	0.175	69.17	1.31
13	0.25	0.25	0.2	68.99	1.27
14	0.25	0.25	0.225	68.38	1.25
15	0.25	0.25	0.25	66.78	1.21

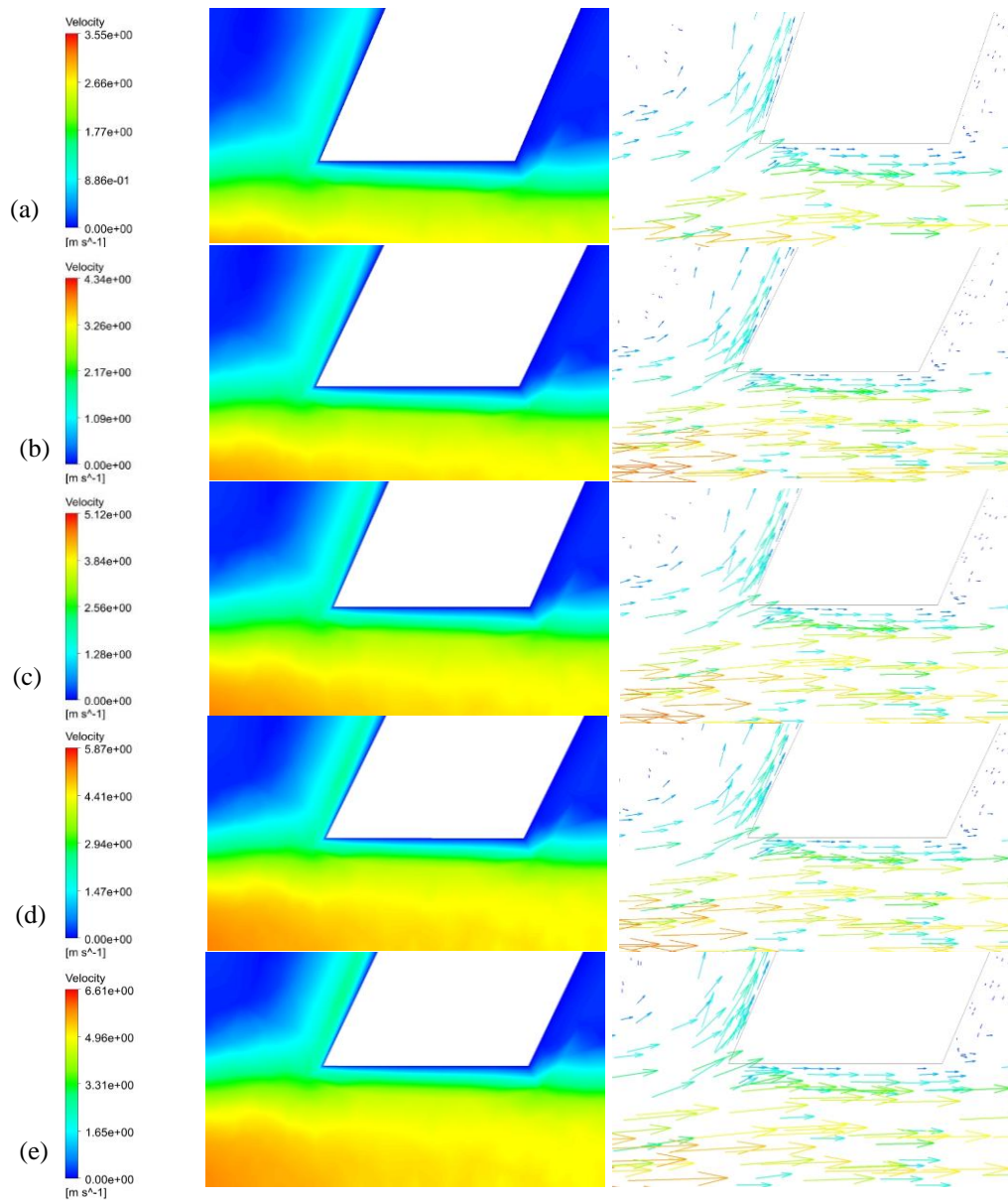


**Fig. 14** Velocity and velocity vector distributions at the front of the rib for different Reynolds number ( $Re$ ) values. (a)  $Re = 442$ ; (b)  $Re = 552$ ; (c)  $Re = 663$ ; (d)  $Re = 773$ ; (e)  $Re = 884$

$$R_{adj}^2 = 1 - \left[ \frac{(1 - R^2)(n - 1)}{(n - k - 1)} \right] \quad (16)$$

where  $n$  is the number of points in a series of data and  $k$  is the number of independent regressors. The  $R_{adj}^2$  was 0.9523 for  $Nu$  and 0.9246 for  $Eu$ .

Figure 15 displays the comparison of  $Nu$  and  $Eu$  between the numerical simulations and fitting correlations in the present work. The maximum errors of  $Nu$  and  $Eu$  appeared at No.10 and No.9, which are 8.75 % and 7.54 %, respectively. And the errors were less than 10%, proving the accuracy of the  $Nu$  and  $Eu$  correlations.

### 5. CONCLUSION

In this paper, the effects of main channel width, branch width and rib width on the  $Nu$  and  $Eu$  values for an SW-MCHS have been examined. Based on the results, the

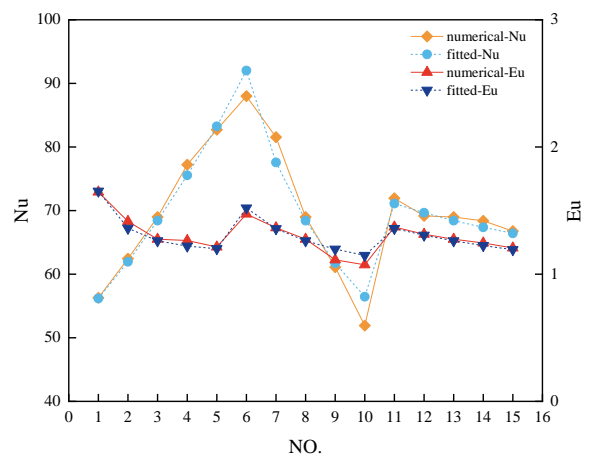


**Fig. 15** Comparison of Nusselt number ( $Nu$ ) and Euler number ( $Eu$ ) values from the numerical simulations and fitting correlations in the present work

$Nu$  and  $Eu$  correlations of the SW-MCHS were fitted. The main research findings are as follows:

(1) An increase in main channel width and a decrease in branch and rib widths can enhance convective heat transfer performance. The influence of main channel width was more significant.

(2) Increases in main channel width, branch width and rib width can reduce  $Eu$  and decrease friction loss. The main channel width had the most significant influence on  $Eu$ , and the rib width had the least significant influence.

(3) The  $R_{adj}^2$  values for the two correlations were 0.9523 and 0.9246, respectively, and the errors were less than 10%, proving the accuracy of the  $Nu$  and  $Eu$  correlations. Consequently, the fitting correlations could be used to predict  $Nu$  and  $Eu$  for the SW-MCHS.

## 6. LIMITATIONS AND FUTURE WORK

The range of  $Re$  selected in our study was 442-884, which could not include all actual working conditions. Therefore, the correlations proposed in this analysis cannot predict  $Nu$  and  $Eu$  beyond the  $Re$  range used in our study. Heat flux will gradually increase in the future, which may impact the correlations proposed in this paper. Experiment study will be conducted in the future plan.

## ACKNOWLEDGEMENTS

The current research was supported by Yunnan Fundamental Research Projects (grant NO. 202201AU07015) and Xingdian Talent Support Program.

## CONFLICT OF INTERESTS

The authors declare that they have no known competing financial interests or personal relationships that could have appeared to influence the work reported in this paper.

## AUTHOR CONTRIBUTIONS

**Lisheng Chen:** Writing of the original draft, software, methodology, data curation. **Yuchi Kang:** Review and editing, supervision, funding acquisition. **Sharon Kao-Walter:** Review and editing.

## REFERENCES

Gao, W., Meng, J., Qu, Z., & Zhang, J. (2024). Experimental and numerical study on thermofluidic characteristics of microchannel heat sinks with various micro pin–fin arrays arrangement patterns. *Applied Thermal Engineering*, 240, 122236. <https://doi.org/10.1016/j.applthermaleng.2023.122236>

Han, X., Liu, H., Xie, G., Sang, L. & Zhou, J. (2021). Topology optimization for spider web heat sinks for electronic cooling. *Applied Thermal Engineering*, 195, 117154. <https://doi.org/10.1016/j.applthermaleng.2021.117154>

Huang, J., Li, L., Yang, J., Affane, H. & Zhang, Q. (2024). Experimental study on the bionic microchannel heat sink integrated with a piezoelectric pump. *Applied Thermal Engineering*, 240, 122282. <https://doi.org/10.1016/j.applthermaleng.2023.122282>

Huang, P., Dong, G., Zhong, X., & Pan, M. (2020). Numerical investigation of the fluid flow and heat transfer characteristics of tree-shaped microchannel heat sink with variable cross-section. *Chemical Engineering and Processing - Process Intensification*, 147, 107769. <https://doi.org/10.1016/j.cep.2019.107769>

Kumar, P. (2019). Numerical investigation of fluid flow and heat transfer in trapezoidal microchannel with groove structure. *International Journal of Thermal Sciences*, 136, 33-43. <https://doi.org/10.1016/j.ijthermalsci.2018.10.006>

Li, J., Cao, Y., Zhu, Z., Shi, L. & Li, J. (2024). Flow and heat transfer characteristics numerical study and structural optimization of bionic homocercal fin microchannels. *CIESC Journal*, 75(05), 1802-1815. <https://doi.org/10.11949/0438-1157.20231069>

Li, J., Zhu, Z., Zhai, H., & Wang, J. (2021). Research progress on heat transfer enhancement and surface drag reduction techniques based on bionics. *Chemical Industry and Engineering Progress*, 40(5), 2375-2388. <https://doi.org/10.16085/j.issn.1000-6613.2020-1140>

Li, P., Guo, D., & Huang, X. (2020). Heat transfer enhancement, entropy generation and temperature uniformity analyses of shark-skin bionic modified microchannel heat sink. *International Journal of Heat and Mass Transfer*, 146, 118846. <https://doi.org/10.1016/j.ijheatmasstransfer.2019.118846>

Li, S., Zhang, H., Cheng, J., Li, X., Cai, W., Li, Z., & Li, F. (2019). A state-of-the-art overview on the developing trend of heat transfer enhancement by single-phase flow at micro scale. *International Journal of Heat and Mass Transfer*, 143, 118476. <https://doi.org/10.1016/j.ijheatmasstransfer.2019.118476>

Lu, G., & Zhai, X. (2019). Analysis on heat transfer and pressure drop of a microchannel heat sink with dimples and vortex generators. *International Journal of Thermal Sciences*, 145, 105986. <https://doi.org/10.1016/j.ijthermalsci.2019.105986>

Niu, Y., Huang, P., & Pan, M. (2021). Study of heat and mass transfer by bionic fractal microchannel plates. *Chemical Engineering & Technology*, 44(4), 741-751. <https://doi.org/10.1002/ceat.202000554>

Pan, M., Wang, H., Zhong, Y., Fang, T. & Zhong, X. (2019). Numerical simulation of the fluid flow and heat transfer characteristics of microchannel heat exchangers with different reentrant cavities. *International Journal of Numerical Methods for Heat*

- & *Fluid Flow*, 29(11), 4334-4348.  
<https://doi.org/10.1108/HFF-03-2019-0252>
- Patil, N. G., & Hotta, T. K. (2018). A review on cooling of discrete heated modules using liquid jet impingement, *Frontiers in Heat and Mass Transfer*, 11. <https://doi.org/10.5098/hmt.11.16>
- Qi, W., Zhao, L., Wang, W., & Liu, Q. (2022). Research progress of high heat flux electronic devices liquid cooling technology. *Science Technology and Engineering*, 22(11), 4261-4270. <https://doi.org/10.3969/j.issn.1671-1815.2022.11.001>
- Rong, Y., Wang, L., Wu, T., Yin, C., Li, X. & Yu, X. (2023). Numerical investigation of heat transfer and parameter coupling characteristics for Spider web microchannel topological structure. *International Journal of Thermofluids*, 17, 100307. <https://doi.org/10.1016/j.ijft.2023.100307>
- Service, R. F. (1998). Coming soon: the pocket DNA sequencer. *Science*, 282(5388), 399-401. <https://doi.org/10.1126/science.282.5388.399>
- Sharma, C. S., Zimmermann, S., Tiwari, M. K., Michel, B. & Poulidakos, D. (2012). Optimal thermal operation of liquid-cooled electronic chips. *International Journal of Heat and Mass Transfer*, 55(7), 1957-1969. <https://doi.org/10.1016/j.ijheatmasstransfer.2011.11.052>
- Sohel Murshed, S. M., & Nieto De Castro, C. A. (2017). A critical review of traditional and emerging techniques and fluids for electronics cooling. *Renewable and Sustainable Energy Reviews*, 78, 821-833. <https://doi.org/10.1016/j.rser.2017.04.112>
- Tan, H., Zong, K., Xiong, C., Weng, X., & Du, P. (2019a). Design and heat transfer performance analysis of leaf vein-shaped microchannel heat sink. *Chinese Journal of Engineering Design*, 26(04), 477-483. <https://doi.org/10.3785/j.issn.1006-754X.2019.04.014>
- Tan, H., Wu, L., Wang, M., Yang, Z., & Du, P. (2019b). Heat transfer improvement in microchannel heat sink by topology design and optimization for high heat flux chip cooling. *International Journal of Heat and Mass Transfer*, 129, 681-689. <https://doi.org/10.1016/j.ijheatmasstransfer.2018.09.092>
- Wang, W., Huang, X., Zhao, F., Chen, S., Wang, L., Cai, Y., & Zhao, Y. (2021a). The performance of vapor chamber based on leaf-vein-like structure for heat dissipation. *Spacecraft Environment Engineering*, 38(2), 138-147. <https://doi.org/10.12126/see.2021.02.004>
- Wang, J., Liu, X., Liu, F., Liu, Y., Wang, F. & Yang, N. (2021b). Numerical optimization of the cooling effect of the bionic spider-web channel cold plate on a pouch lithium-ion battery. *Case Studies in Thermal Engineering*, 26, 101124. <https://doi.org/10.1016/j.csite.2021.101124>
- Wu, L., Lu, T., Chen, J., Wang, Y., & Du, P. (2018). A study of bionic micro-channel topology for chip cooling. *Acta Electronica Sinica*, 46(5), 1153-1159. <https://doi.org/10.3969/j.issn.0372-2112.2018.05.020>
- Wu, T., Wang, L., Tang, Y., Yin, C., & Li, X. (2022). Flow and heat transfer performances of liquid metal based microchannel heat sinks under high temperature conditions. *Micromachines*, 13(1), 95. <https://doi.org/10.3390/mi13010095>
- Yang, W., Zhou, F., Liu, Y., Xu, S., & Chen, X. (2021). Thermal performance of honeycomb-like battery thermal management system with bionic liquid mini-channel and phase change materials for cylindrical lithium-ion battery. *Applied Thermal Engineering*, 188, 116649. <https://doi.org/10.1016/j.applthermaleng.2021.116649>
- Yao, F., Guan, X., Chen, Q., & Lin, L. (2024). Research on thermal management system of lithium-ion battery with a new type of spider web liquid cooling channel and phase change materials. *Journal of Energy Storage*, 81, 110447. <https://doi.org/10.1016/j.est.2024.110447>
- Zhang, F., Huang, Z., Li, S., Sun, S., & Zhao, H. (2024a). Design and thermal performance analysis of a new micro-fin liquid cooling plate based on liquid cooling channel finning and bionic limulus-like fins. *Applied Thermal Engineering*, 237, 121597. <https://doi.org/10.1016/j.applthermaleng.2023.121597>
- Zhang, F., Wang, F., Zhu, Y., & He, Y. (2024b). Structural optimization of thermal management system for bionic liquid cold battery based on fuzzy grey correlation analysis. *Applied Thermal Engineering*, 249, 123347. <https://doi.org/10.1016/j.applthermaleng.2024.123347>
- Zhu, G., Liu, S., Zhang, D., Chen, W., Li, J., & Wen, T. (2024). Transfer learning model to predict flow boiling heat transfer coefficient in mini channels with micro pin fins. *International Journal of Heat and Mass Transfer*, 220, 125020. <https://doi.org/10.1016/j.ijheatmasstransfer.2023.125020>